Far-field coseismic forcing of giant rockslides in the 2017 Sarpol-Zahab Earthquake (Iran)

Aya Cheaib[1], Pascal Lacroix[2], Swann Zerathe[3], Denis Jongmans[4], najmeh ajorlou[5], Marie-Pierre Doin[6], James Hollingsworth[1], and Chadi Abdallah[7]

[1]Université Grenoble Alpes
[2]ISTerre/IRD/UGA/CNRS
[3]ISTerre
[4]Grenoble University
[5]2Department of earth science, Institute for Advanced Studies in Basic Sciences(IASBS)
[6]Institut des Sciences de la Terre
[7]CNRS

November 26, 2022

Abstract

On November 12th 2017, the largest earthquake (Mw 7.3) ever recorded in the Zagros mountains occurred near the town of Sarpol-Zahab, Iran. While this region encompasses clusters of giant ancient rockslides, this seismic event is an excellent case-study to decipher the controlling factors of earthquake-induced landslides. Here, we address this issue by deriving an original earthquake-induced landslide inventory, encompassing landslides of various velocities (from rapid rockfalls to slow-moving landslides). This inventory displays clear differences in the spatial and volumetric distributions of earthquake-induced landslides, with 360 rockfalls triggered around the epicenter, and 9 giant active and ancient rockslides coseismically accelerated at locations up to 180 km from the epicenter. This distant triggering is explained by the earthquake source properties coupled with the local geological conditions. Our study documents a rare example of slow-moving landslides accelerated by an earthquake, and opens perspectives for the study of the landslide triggering over various time-scales.

Far-field coseismic forcing of giant rockslides in the 2017 Sarpol-Zahab Earthquake (Iran)

Aya Cheaib[1,3], Pascal Lacroix[1], Swann Zerathe[1], Denis Jongmans[1], Najmeh Ajorlou[2], Marie-Pierre Doin[1], James Hollingsworth[1], and Chadi Abdallah[3]

[1]ISTerre - Université Grenoble Alpes, IRD, CNRS, IFSTTAR, Université Savoie Mont Blanc, CS 40700, 38058 GRENOBLE Cedex 9 Grenoble, France.

[2]Department of earth science, Institute for Advanced Studies in Basic Sciences(IASBS), 444 Prof. Yousef Sobouti Blvd., Zanjan 45137-66731, Iran.

[3]Lebanese National Council for Scientific Research/Remote Sensing Center, Blvrd Sport City, Bir Hassan, P.O. Box 11-8281, Beirut, Lebanon.

Corresponding author: Aya Cheaib (aya.cheaib@univ-grenoble-alpes.fr)

Key Points:

- Novel approach for generating a comprehensive earthquake-induced landslide inventory (by combining various satellite data and methods).
- The forcing of several giant pre-existing rockslides in the far-field (140 to 180 km) of the Sarpol-Zahab earthquake epicenter.

Abstract

On November 12th 2017, the largest earthquake (Mw 7.3) ever recorded in the Zagros mountains occurred near the town of Sarpol-Zahab, Iran. While this region encompasses clusters of giant ancient rockslides, this seismic event is an excellent case-study to decipher the controlling factors of earthquake-induced landslides. Here, we address this issue by deriving an original earthquake-induced landslide inventory, encompassing landslides of various velocities (from rapid rockfalls to slow-moving landslides). This inventory displays clear differences in the spatial and volumetric distributions of earthquake-induced landslides, with 360 rockfalls triggered around the epicenter, and 9 giant active and ancient rockslides coseismically accelerated at locations up to 180 km from the epicenter. This distant triggering is explained by the earthquake source properties coupled with the local geological conditions. Our study documents a rare example of slow-moving landslides accelerated by an earthquake, and opens perspectives for the study of the landslide triggering over various time-scales.

Plain Language Summary

Landslides are one of the main secondary effects of earthquakes, with up to several thousands of landslides triggered during large magnitude earthquakes. The spatial and size distribution of these landslides is function of the earthquake source and site specificities. The factors that control earthquake-induced landslides can be diverse and combine in complex ways. In this study, we address this issue by focusing on the landslides induced by the Mw7.3 Sarpol-Zahab earthquake that struck the Zagros mountains (Iran/Irak border) on November 12th 2017. We developed an original approach to detect and monitor landslides of different velocities, from rapid rockfalls (m/s) to slow-moving landslides (m/yr to mm/yr), by using a set of various satellite data and techniques. The striking elements of our landslide inventory is (1) the very little number of slope movements induced by the shaking, and (2) the unprecedented detection of giant rockslides (~ 10^9 m^3) in the far-field of an earthquake. This distant triggering is explained by a combination of the earthquake source properties coupled with the local geological conditions. These giant and slow-moving landslides, which have probably been active for several millennia, are unique objects for the study of earthquake forcing on landslides over time.

1 Introduction

Slope failures are one of the main secondary effects of earthquakes (Marano et al., 2010), with a large part of co- and post-seismic damage caused by landslides in mountainous areas (Fan et al., 2019; Keefer, 2002; Marc et al., 2015). Many factors can contribute to the heterogeneous spatial distribution of earthquake-induced landslides: geology (Roback et al., 2018), topography (Meunier et al., 2008), groundwater (e.g., Wang et al., 2014), and earthquake source characteristics (e.g., Gorum et al., 2011). In addition, shaking can have delayed effects on slope stability at time scales from days to years. These effects may include changes in groundwater circulation (Wang & Chia, 2008), a modification in soil permeability (Rojstaczer & Wolf, 1992), or a degradation of the mechanical properties of the slope thereby making it more susceptible to landslides in future earthquakes (Bontemps et al., 2020; Marc et al., 2015). The quantification of these controlling factors and their subsequent mechanisms is, however, based on a limited number of earthquake-induced landslide inventories (e.g. Tanyas et al., 2017), and on the instrumentation of a small number of low-velocity active landslides in seismic areas (Bontemps et al., 2020; Lacroix et al., 2014), thus highlighting the need to document and analyze more earthquake-induced landslides across a wider range of seismic and climatic settings.

On November 12th 2017, a Mw7.3 earthquake struck the northwestern part of the Zagros Mountains, close to the town of Sarpol-Zahab (Figure 1). This major earthquake occurred at the end of the dry season in a semi-arid area that encompasses a high density of giant paleo-landslides of volumes between 0.01-30 km^3 affecting mostly carbonate lithology (Ghazipour & Simpson, 2016). Following this earthquake, a few coseismic landslides of various types (debris fall, boulder/rock fall) were reported near the epicenter (Miyajima et al., 2018; Vajedian et al., 2018). The earthquake triggered the giant Mela-Kabod landslide (4-km-long, 1-km-wide) ~40 km south of the epicenter, with a coseismic displacement of ~30 m (Goorabi, 2020; Vajedian et al.,2018). No reactivation was reported for the many other giant landslides in this region.

The large Sarpol-Zahab earthquake provides a unique opportunity to study the forcing mechanisms of landslides under strong seismic stressing in a semi-arid region. To this end, we have used optical satellite and multi-temporal InSAR methods to establish a complete inventory of rapid (~m/s) and slow (~mm to m/yr) landslides and investigate their response to the earthquake.

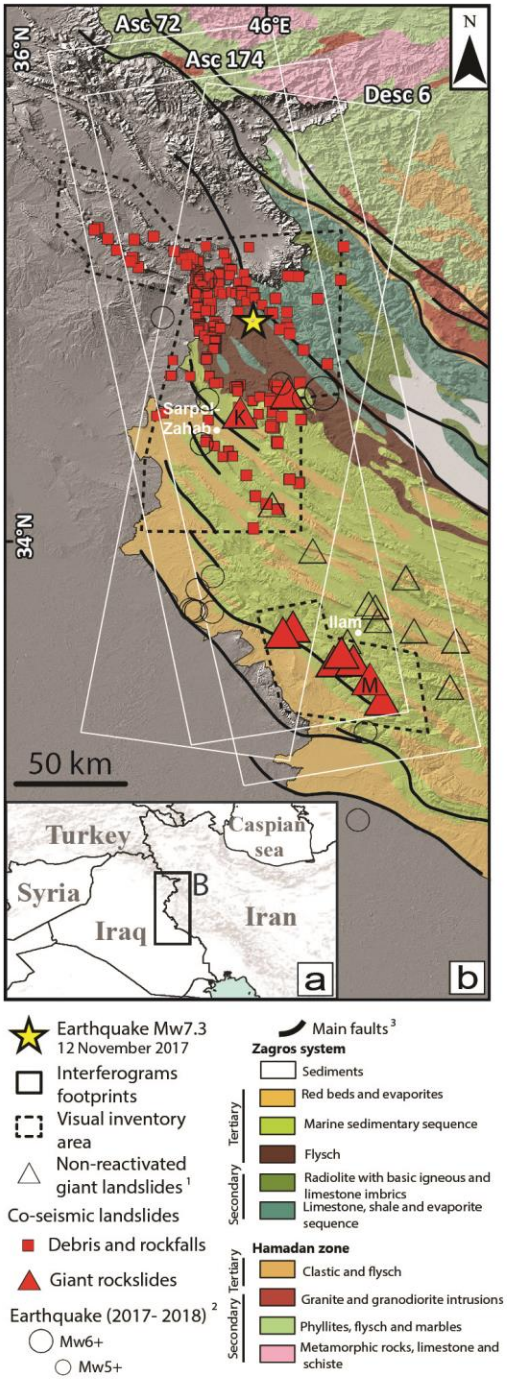

Figure 1. (a) Study area location. (b) Coseismic landslide inventories (geology adapted from the 1:2,500,000 tectonic map of the National Iranian Oil Company, 1978). Empty triangles correspond to giant landslides mapped by Ghazipour and Simpson (2016). The landslides most mentioned in this study are the Mela-Kabod landslide (K) and the Mehr rockslide (M).

Earthquakes (Mw>5; period 2017-2018) are reported from [2]US Geological Survey. The main faults are from [3]Hessami et al. (2003).

2 Geological settings

The Zagros fold and thrust belt (ZFTB, Figure 1) formed in response to the collision between the Arabian and Eurasian plates, which initiated at ~35 Ma (McQuarrie et al., 2003) and continues at the present day with a convergence rate of 8-23 mm/yr (Masson et al., 2014). This N-S convergence produced (1) a succession of asymmetrical, NW-trending, inverted folds affecting a 7-12 km thick pile of sedimentary rocks, comprising limestones, siltstones, shales and salts dating from the Cenozoic to Palaeozoic, and (2) major NW-striking active thrust faults associated with significant seismicity (Mw>6) at the interface between basement and sedimentary cover units at ~20 km depth (Figure 1b; Tavani et al., 2018). The high relief of the Zagros, culminating at about 3650 m altitude, is strongly controlled by resistant calcareous anticlines, which form a succession of ridges separated by narrow valleys developed along the synclinal axes. This semi-arid zone receives about 230 mm/yr of rainfall annually, which falls mostly between November and May. The Mw7.3 Sarpol-Zahab earthquake (12/11/2017) occurred along a near-horizontal blind thrust fault, located between 14-20 km depth (Barnhart et al., 2018; Chen et al., 2018; Gombert et al., 2019; Nissen et al., 2019). Previous studies inferred: (1) a fault rupture of ~50-km-long and ~30-km-wide with a maximum coseismic slip of 5.5 ± 0.5 m, and (2) a high impulsive source with a robust southward rupture directivity which produced the largest ground motions (PGA = ~700 cm/s^2) in the Sarpol-Zahab town (~40 km south from the epicenter). Moreover, high horizontal peak ground accelerations (~100 cm/s^2) were recorded up to 100 km south of the source (Mahani & Kazemian, 2018).

3 Materials and Methods

3.1 Optical Satellite Images Comparison and Correlation

A detailed coseismic landslide inventory was conducted by the visual comparison of PlanetScope satellite images (3 m resolution) acquired before and after the earthquake (19/10/2017 and 13/11/2017) covering an area of 12,000 km^2 centered on the epicenter (see footprint on Figure 1 and Figure S1 in the supporting information). We typically detected and mapped new rockfall scars and debris deposits induced by the earthquake. We also calculated earthquake-induced horizontal ground displacement from the correlation of pre/post-earthquake optical satellite images (Leprince et al., 2007), using both SPOT6/7 images (orthorectified at 1.5 m resolution, following Beyer et al. (2018) see Section S1 for further details), and PlanetScope satellite images-see Table S1, Figure S1, and text S1.

3.2 InSAR Processing

To detect and monitor smaller ground motions associated with earthquake-induced slow-moving landslides, we derived Sentinel-1 InSAR time-series (Doin, et al., 2011) for each landslide using 72 Sentinel-1 SAR images spanning a 20 month time period (beginning 10 months before the earthquake). We generated differential interferograms using the NSBAS (New Small BAseline Subset) (Doin et al., 2011) processing chain based on the ROI_PAC software (Rosen et al., 2004). We used two ascending (174 and 72, subswath iw1 for both) and one descending (6, subswath iw2) tracks of Sentinel 1A and 1B covering an area of 33,500 km2 (see footprint on Figure 1b and Table S1), with a revisit time of 12 days. Initially, we re-sampled all secondary SLC (Single Look Complex) images in a single reference SLC geometry and co-registered secondary to reference using precise orbits and an ASTER digital elevation model (30 m resolution), combined with empirical offsets between secondary and reference images. Then, a small baseline subset is defined using temporal and perpendicular baseline constraints (Doin, et al., 2011). After calculating differential interferograms we corrected them from atmospheric delays using ERA-5 ECMWF reanalysis (Doin et al., 2009). Finally, we made an empirical correction for topographically-correlated atmospheric-delays. The coseismic interferograms were then inspected for landslide-like patterns throughout the region. The coseismic signals were too large to be unwrapped due to phase ambiguities across landslide boundaries. For this reason, we bound the amplitude of the coseismic motion using (1) the number of fringes on the coseismic interferogram (which provides a lower limit), and (2) the optical image correlation (an upper limit). For the same reason, we also analyze the time-series independently to determine the pre- and post- seismic landslide kinematics (see text S5).

3.3 Geomorphological Analysis

Finally, we conducted geomorphological and geological analysis coupling the stereo-derived high resolution DEMs (text S1), Google Earth satellite imagery and geological maps to better constrain the typology and failure modes of the detected landslides.

4 Results

4.1 Rockfalls

We map 360 coseismic rockfalls, and their associated debris cones (areas ranging between 200- and 20,000 m^2), which affect mainly limestones and flyschs (Figure 1b, S2). About 85% of the detected rockfalls are concentrated within a radius of 40 km (smaller than the fault rupture length) of the epicenter (Figure S3). They mostly occurred on slopes between 40° and 80°, which are significantly steeper than the mean ~18° slope of the area (Figure S4).

4.2 Giant rockslides

4.2.1 Coseismic Detection

Nine instances of coseismic landslide motion were detected (Figure 1b), one from the coseismic correlation of optical images (Mela-Kabod) and eight from the coseismic interferograms analysis (areas between 2-15 km^2, see Table S2). They are all located south of the epicenter, two at ~40 km , and the remaining seven clustered between 140-180 km from the epicenter (Figure 1b, Table S2), in a region where no rapid slope-failures were detected in the PlanetScope imagery. The giant Mela-Kabod landslide displays a coseismic motion of about 35 m (Figure S5), a value consistent with previous estimates (Valkaniotis et al., 2018).

InSAR analysis reveals activity of 8 landslides, which are generally characterized by 3-4 fringes outlined by sharp phase discontinuities with the surrounding area (Figure 2) during the coseismic period. They correspond to a coseismic motion of at least 30 mm in the Line Of Sight (LOS), reaching more than 100 mm in most cases (Figure 2b, c, Table S2 and text S4). Four of the detected patterns are correlated with giant rockslides from the inventory of Ghazipour and Simpson (2016); the other four reflect newly mapped slope failures (Table S2).

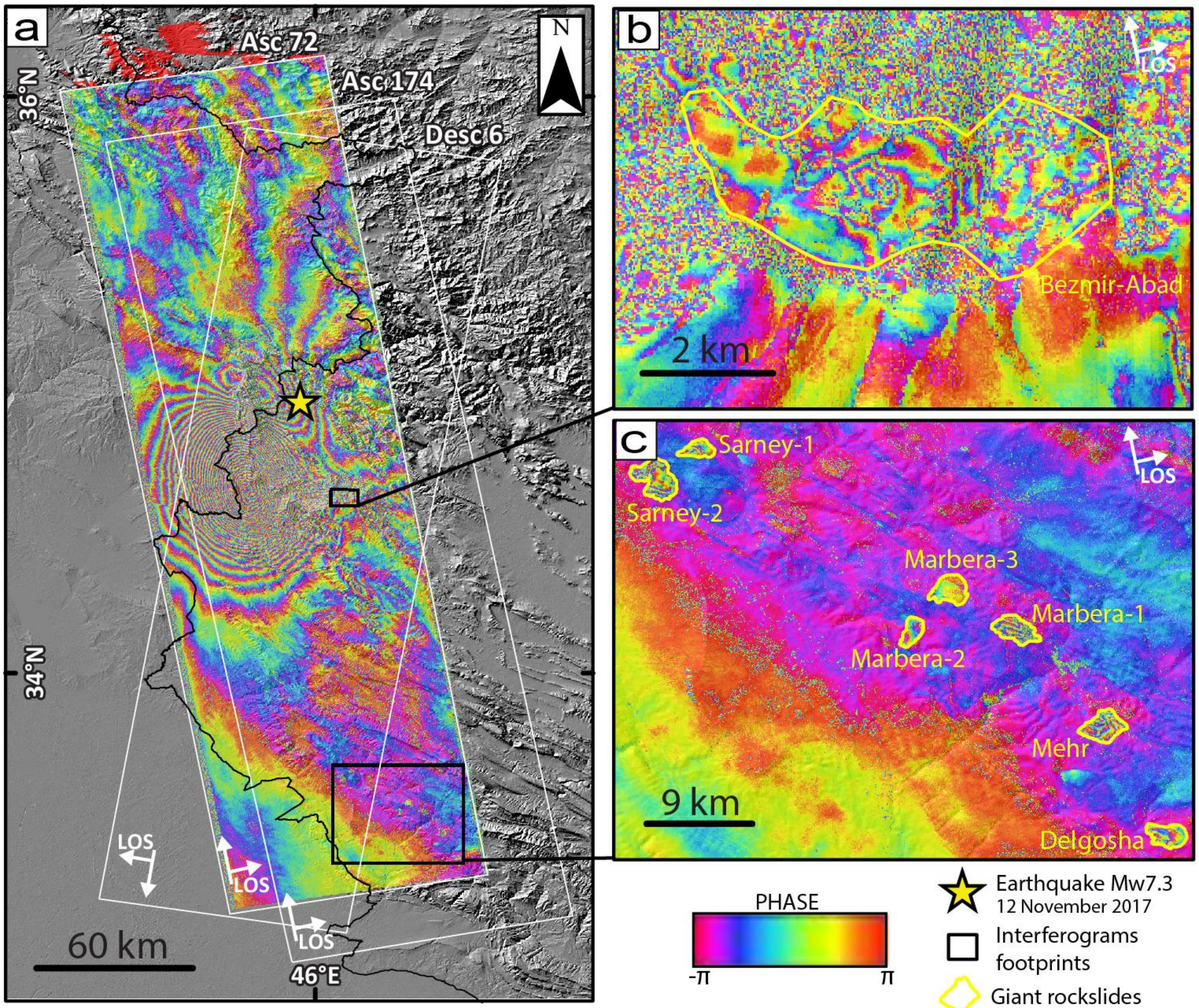

Figure 2. (a) Example of a coseismic interferogram computed over the study area from the ascending track 72 between 11/11/2017 and 17/11/2017 (the looking angle of the radar varies between 27.3°-32.5°). (b) and (c) zooms show the 8 landslides detected with InSAR near the earthquake and in the southern far-field, respectively.

4.2.2 Annual kinematics

The cumulative LOS displacement time-series computed shows different pre- and post-seismic rockslide behaviors. Rockslide velocities range between 0-25 mm/yr, and 2-46 mm/yr for the pre- and post-seismic periods, respectively (Figure 3 and Table S2). The pre-seismic period shows either dormant rockslides (almost zero velocity within the error limits: Figure 3c, d, e, h) or active rockslides with constant velocities (Figure 3b, f, g, i, j). The coseismic motion is followed by a transient relaxation over 20 days clearly seen at several sites: Mela-Kabod, Marbera-3, Marbera-1 and Mehr (Figure 3c, f, g, i). Following this, three different post-seismic patterns emerge: (1) rockslides with constant post-seismic velocity equivalent to the pre-seismic one (Figure 3b, d, h, i), (2) rockslides with constant post-seismic velocity higher than the pre-seismic one (Figure 3e, j) and (3) rockslides showing a transient increase in velocity of several months before returning to their pre-seismic rates (Figure 3c, f, g). In this latter case, the succession of those two ultimate post-seismic phases coincides with the rainy and dry seasons as shown by the comparison with cumulated rainfall (Figure 3a). Finally, an offset of the last acquisition date at the end of the Bezmir Abad time-series (Figure 3b) may correspond to the co-seismic effects of a Mw6.0 earthquake that occurred 13 kilometers away (Figure 1, S7).

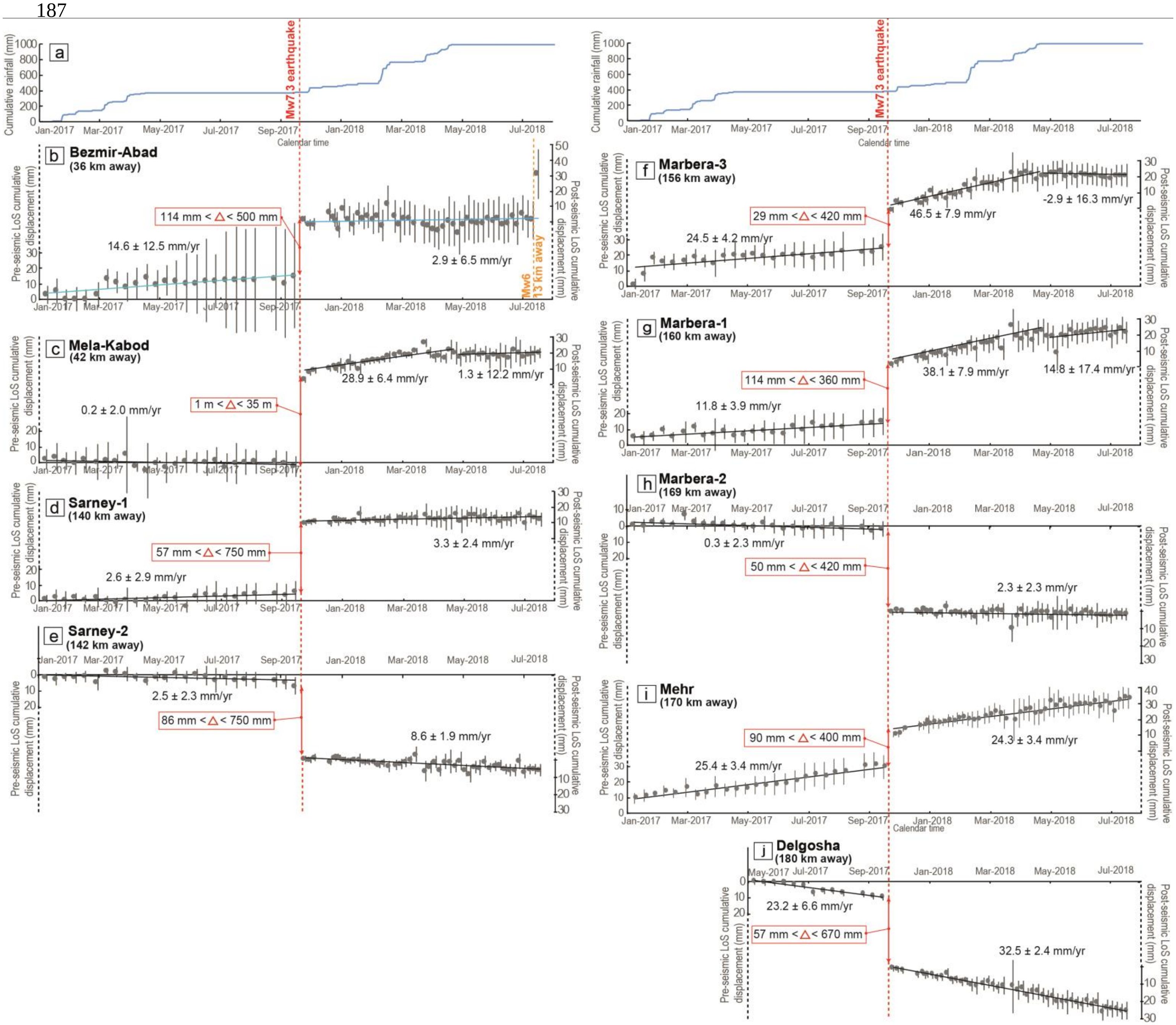

Figure 3. (a) Cumulative rainfall collected at the Ilam meteorological station (Figure 1b; National Climatic Data Center). (b) to (j) show the cumulative LOS displacement time-series with the error bars, computed for all the detected rockslides from InSAR over 18 months spanning the Mw7.3 Sarpol-Zahab earthquake and revealing the rockslide coseismic motion (Δ). The pre-

seismic InSAR time-series for the Delgosha rockslide (j) span for only 6 months before the earthquake.

4.2.2 Geomorphological characterization

Results from our geomorphological analysis of the Mehr rockslide, located 170 km south of the epicenter, are shown in Figure 4 (see Figure S6 and table S2 for detailed results of the other rockslides). The coseismic motion extent, clearly visible in the interferogram (Figure 4a), delineates a region 3 km long by 2.5 km wide, which is bounded to the SW by a ~160 m high headscarp and to the northeast by the toe of debris deposits that propagate ~600 m over the valley floor (see DEM in Figure 4b). At the SE limit, the lateral rockslide boundary is well-defined in the geomorphology. The geological map (Figure 4c) and the cross-section (Figure 4d) indicate that the rockslide occured at the contact between Ilam limestones and overlying Surgah shales, along the northern flank of a NW-SE-striking anticline. The rockslide consists of limestone blocks sliding on the shale layer, which dips 5-15° to the NE. Comparison between a topographic profile extracted along the rockslide and another along the undisturbed slope suggests a maximum depth of 200 m for the slip surface (Figure 4d), implying a rockslide volume of ~0.5 km^3.

Observations are similar for the other rockslides (Figure S6 and Table S2): (1) all the detected interferometric patterns match the positions of pre-existing giant rockslides with an estimated volume range from 0.16 to 2.2 km^3, and (2) six of those rockslides occur at the contact between limestone and shales from the Ilam and the Surgah formations.

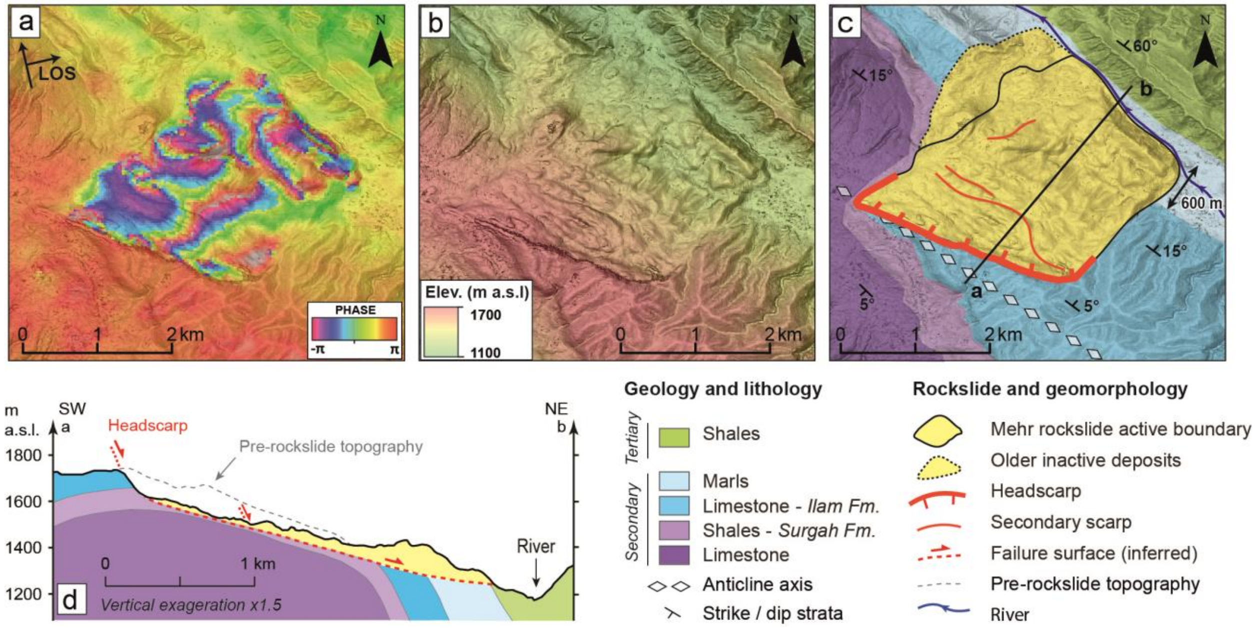

Figure 4. The Mehr giant rockslide (see location in Figure 1b) presented from (a) a coseismic interferogram computed along the Sentinel-1 ascending track-72 between 11/11/2017 and 17/11/2017, (b) a pre-seismic SPOT6-7 hillshaded DEM (4 m resolution, 09/09/2014), (c) a geological map adapted from Llewellyn (1974), (d) a cross-section built along the profile “ab” shown in c.

5 Discussion

5.1 Coseismic landslide database

The Sarpol-Zahab earthquake induced coseismic displacements for two types of landslides: 360 small rockfalls clustered in a radius of a few tens of kilometers around the epicenter, and 9 giant rockslides mainly located in the far-field (up to 4 times the fault length). The high concentration of rockfalls in the epicentral area (compared to the wider zone of fault slip) can be explained by the impulsive source (Gombert et al., 2019), which leads to stronger ground-motions close to the epicenter. This spatial distribution highlights the dynamic triggering of these rockslides (e.g., Meunier et al., 2007).

The number of recorded landslides is low for a Mw7.3 earthquake, which would be expected to trigger a few thousand landslides in such a mountainous area (Keefer, 2002, Tanyas et al., 2017). This low number may be explained by (1) the aridity of the region, which limits weathering and soil production (Lacroix et al., 2013, Roback et al., 2018), and (2) blind thrust faulting, which induces lower ground motions than surface rupturing earthquakes (Aki, 1987).

5.2 Far-field seismic forcing

The striking feature of this earthquake resides in the coseismic motion of several giant pre-existing rockslides located at epicentral distances of 140 km to 180 km (Figure 1b). Keefer (2002) documents several case studies where small landslides were triggered at large distances from the epicenters, possibly due to low seismic attenuation and/or extraordinary susceptibility of some sites. However, the huge size (~0.1-2 km^3) of the earthquake-induced rockslides here is intriguing and, to our knowledge, has never been reported so far from the epicenter.

Rockslide forcing in the far field south of the epicenter can first be explained by the strong directivity of the rupture toward the south (Chen et al., 2018; Gombert et al., 2019), as well as by the stronger movements perpendicular to the fault (Mahani & Kazemian, 2018), which may favor the triggering of rockslides oriented NE-SW. In the ZFTB geological context, the ground shaking can also be amplified by both local topographic and geological effects (Maufroy et al., 2015; Murphy, 2015), more specifically as the rockslides developed on flanks of anticline ridges and in mechanically heterogeneous lithologies. Calculation of a 1D resonance frequency of the destructured slump body overlying the thick rigid layer shows wave amplifications at low frequencies (text S6), around 1Hz, compatible with the frequency content of the earthquake source at such large distances (Mahani & Kazemian, 2018), which can thus favor landslide triggering.

Interestingly, several other ancient landslides previously mapped in this region (Ghazipour & Simpson, 2016) were not reactivated during the Sarpol-Zahab earthquake (Figure 1b). However, these landslides mostly occurred in different lithologies (Oligocene and Eocene units) with a structure (thick moderately incompetent layer of calcareous shale underlying the carbonate slump body) less sensitive to sliding and seismic amplification.

Finally, our time-series reveal a transient increase of the post-seismic velocity compared to the pre-seismic annual velocity for at least 5 of the studied rockslides (Figure 3c, e, f, g, j). For 3 of the rocksldies (Mela-Kabd, Marbera-1, Marbera-3) we document a higher velocity during the 2018 rainy season (Figure 3c, f, g) followed by a subsequent decrease in velocity, eventually returning to the pre-earthquake velocity during the dry season. This observation may suggest a seasonal motion and threshold rainfall effects on the landslide kinematics (Zerathe et al., 2016). Furthermore, moderate earthquakes (Mw5-6) that occurred close to the landslides (Figure 1, S7) may have contributed to the transient velocity increase by damaging rock, thus promoting water infiltration (Bontemps et al., 2020) up to the impermeable Surgah formation. However, exploring these issues will require longer time-series as well as detailed field measurements of hydrologic and kinematical parameters (e.g. Schulz et al., 2009).

6 Conclusion

We used a new approach to generate a comprehensive inventory of earthquake-induced landslides, combining InSAR, image correlation and visual change detection. Applying it to the Mw 7.3 Sarpol-Zahab earthquake, we detected 369 coseismic landslides of different sizes and kinematics, including 360 rockfalls and 9 giant rockslides.

The striking element of this earthquake-induced landslide database is the coseismic motion of 9 pre-existing giant rockslides (3-30 km^2) in the far field, all initially generated by sliding of a thick limestone layer over a shale formation on both limbs of anticlinal structures, in directions perpendicular to the anticline axis (i.e. NE-SW). The coseismic motion of these slow-moving giant rockslides (<40 mm/yr) was at least 30 mm, reaching up to 35 m. At least three of them were also accelerated over the rainy season following the earthquake, showing either a seasonal climatic forcing or an increased rainfall infiltration enhanced by the landslide bulk damage produced by the ground shaking. We show that the coseismic motion of these rockslides may be related to a complex combination of the southward directivity of the source, the NE-SW polarization of the motions, their sensitivity to low-frequencies (~1 Hz), and the site effect due to the seismic impedance contrast on the flanks of the anticlines.

The detection of significant coseismic motion of several ancient giant rockslides using InSAR may open new perspectives on the understanding of large-scale gravitational deformations in arid settings. Most of the rockslides investigated here display huge cumulated headscarps (100’s m); it is therefore likely that repeated large earthquakes over longer time scales constitute one of the predominant forcings for this displacement. These landslides have certainly been active over several millennia, as observed for other giant landslides of the area (Roberts & Evans, 2013). Dating of landslide headscarps is therefore a key issue in understanding how earthquakes control landslide dynamics on different time scales.

Acknowledgments, Samples, and Data

This research is funded by the Lebanese National Council for Scientific Research (CNRS). The authors also thank the support of the French Spatial Agency (CNES). Supplementary figures, tables and graphs are provided in the supporting information accompanying the main text. The

data archiving is underway on the PerSCiDO platform. Meanwhile, the data are available at the following link https://1drv.ms/u/s!Alv20Xzpi7Jig2gksQk9RHNuN3Ym?e=AanU5p.

References

Aki, K., 1987, Strong Motion Seismology, *in* Erdik, M.Ö., Toksöz, M.N. (eds), *Strong Ground Motion Seismology* (Vol. 204). Dordrecht:Springer. https://doi.org/10.1007/978-94-017-3095-2_1.

Barnhart, W. D., Brengman, C. M., Li, S., & Peterson, K. E. (2018), Ramp-flat basement structures of the Zagros Mountains inferred from coseismic slip and afterslip of the 2017 Mw7. 3 Darbandikhan, Iran/Iraq earthquake. Earth and Planetary Science Letters, 496, 96-107. https://doi.org/10.1016/j.epsl.2018.05.036.

Beyer, R. A., Alexandrov, O., & McMichael, S. (2018), The Ames Stereo Pipeline: NASA's open source software for deriving and processing terrain data. Earth and Space Science, 5(9), 537-548. https://doi.org/10.1029/2018EA000409.

Bontemps, N., Lacroix, P., Larose, E., Jara, J., & Taipe, E. (2020), Rain and small earthquakes maintain a slow-moving landslide in a persistent critical state. Nature communications, 11(1), 1-10. doi:10.1038/s41467-020-14445-3.

Chen, K., Xu, W., Mai, P. M., Gao, H., Zhang, L., & Ding, X. (2018), The 2017 Mw 7.3 Sarpol Zahāb Earthquake, Iran: A compact blind shallow-dipping thrust event in the mountain front fault basement. Tectonophysics, 747, 108-114. https://doi.org/10.1016/j.tecto.2018.09.015.

Doin, M.P., Guillaso, S., Jolivet, R., Lasserre, C., Lodge, F., Ducret, G., & Grandin, R. (2011), Presentation of the small baseline NSBAS processing chain on a case example: the Etna deformation monitoring from 2003 to 2010 using Envisat data. Proceedings of the Fringe symposium, Frascati, Italy: ESA SP-697, 3434-3437.

Doin, M.-P., Lasserre, C., Peltzer, G., Cavalie, 0., & Doubre, C. (2009), Corrections of stratified tropospheric delays in SAR interferometry: Validation with global atmospheric models. *Journal of Applied Geophysics, 69(1),* 35-50. doi:10.1016/j.jappgeo.2009.03.010.

Fan, X., Scaringi, G., Korup, O., West, A. J., Van Westen, C. J., Tanyas, H., et al. (2019), Earthquake-induced chains of geologic hazards: Patterns, mechanisms, and impacts. *Reviews of geophysics, 57(2),* 421-503. https://doi.org/10.1029/2018RG000626.

Ghazipour, N., & Simpson, G. (2016), Size distribution and controls of landslides in the Zagros mountain belt (Iran). *Geological Society of America Special Papers, 525.* doi: 10.1130/2016.2525(13).

Gombert, B., Duputel, Z., Shabani, E., Rivera, L., Jolivet, R., & Hollingsworth, J. (2019), Impulsive Source of the 2017 MW= 7.3 Ezgeleh, Iran, Earthquake. *Geophysical research letters, 46(10),* 5207-5216. https://doi.org/10.1029/2018GL081794.

Goorabi, A. (2020), Detection of landslide induced by large earthquake using InSAR coherence techniques–Northwest Zagros, Iran. *The Egyptian Journal of Remote Sensing and Space Science, 23(2),* 195-205. https://doi.org/10.1016/j.ejrs.2019.04.002.

Gorum, T., Fan, X., Van Westen, C. J., Huang, R. Q., Xu, Q., Tang, C., & Wang, G. (2011), Distribution pattern of earthquake-induced landslides triggered by the 12 May 2008 Wenchuan earthquake. *Geomorphology, 133(3-4),* 152-167. https://doi.org/10.1016/j.geomorph.2010.12.030.

Hessami, K., Jamali, F., & Tabassi, H. (2003), *Map of major active faults of Iran* (scale 1: 2,500,000).

Keefer, D. K. (2002), Investigating landslides caused by earthquakes–a historical review. *Surveys in geophysics, 23(6),* 473-510. https://doi.org/10.1023/A:1021274710840.

Lacroix, P., Perfettini, H., Taipe, E., & Guillier, B. (2014), Coseismic and postseismic motion of a landslide: Observations, modeling, and analogy with tectonic faults. *Geophysical Research Letters, 41(19)*, 6676-6680. https://doi.org/10.1002/2014GL061170.

Lacroix, P., Zavala, B., Berthier, E., & Audin, L. (2013), Supervised method of landslide inventory using panchromatic SPOT5 images and application to the earthquake-triggered landslides of Pisco (Peru, 2007, Mw8. 0). *Remote Sensing, 5(6)*, 2590-2616. doi:10.3390/rs5062590.

Leprince, S., Ayoub, F., Klinger, Y., & Avouac, J.P. (2007), Co-registration of optically sensed images and correlation (COSI-Corr): An operational methodology for ground deformation measurements. *International Geoscience and Remote Sensing Symposium IEEE, Barcelona,* 1943-1946. doi:10.1109/IGARSS.2007.4423207.

Llewellyn, P.G. (1974). Geological compilation map, Ilam-Kuhdasht (Map NO.20504). Tehran:Oil Service Company of Iran.

Mahani, A. B., & Kazemian, J. (2018), Strong ground motion from the November 12, 2017, M 7.3 Kermanshah earthquake in western Iran. *Journal of Seismology, 22(6)*, 1339-1358. https://doi.org/10.1007/s10950-018-9761-x.

Marano, K. D., Wald, D. J., & Allen, T. I. (2010), Global earthquake casualties due to secondary effects: a quantitative analysis for improving rapid loss analyses. *Natural hazards, 52(2),* 319-328. doi:10.1007/s11069-009-9372-5.

Marc, O., Hovius, N., Meunier, P., Uchida, T., & Hayashi, S. (2015), Transient changes of landslide rates after earthquakes. *Geology, 43(10)*, 883-886. https://doi.org/10.1130/G36961.1.

Masson, F., Lehujeur, M., Ziegler, Y., & Doubre, C. (2014), Strain rate tensor in Iran from a new GPS velocity field. *Geophysical Journal International*, *197(1)*, 10-21. https://doi.org/10.1093/gji/ggt509.

Maufroy, E., Chaljub, E., Hollender, F., Kristek, J., Moczo, P., Klin, P., et al. (2015), Earthquake Ground Motion in the Mygdonian Basin, Greece: The E2VP Verification and Validation of 3D Numerical Simulation up to 4 Hz. *Bulletin of the Seismological Society of America, 105(3),* 1398–1418. doi: 10.1785/0120140228.

McQuarrie, N., Stock, J.M., Verdel, C., & Wernicke, B.P. (2003), Cenozoic evolution of Neotethys and implications for the causes of plate motions. *Geophysical research letters, 30(20),* SDE 6.1-SDE 6.4. doi:10.1029/2003GL017992.

Meunier, P., Hovius, N., & Haines, A.J. (2007), Regional patterns of earthquake-triggered landslides and their relation to ground motion. *Geophysical Research Letters, 34(20),* L20408. doi:10.1029/2007GL031337.

Meunier, P., Hovius, N., & Haines, J.A. (2008), Topographic site effects and the location of earthquake induced landslides. *Earth and Planetary Science Letters, 275(3-4),* 221-232. https://doi.org/10.1016/j.epsl.2008.07.020.

Miyajima, M., Fallahi, A., Ikemoto, T., Samaei, M., Karimzadeh, S., Setiawan, H., et al (2018), Site investigation of the Sarpole-Zahab earthquake, Mw 7.3 in SW Iran of November 12, 2017. *JSCE Journal of Disaster, FactSheet: FS2018-E-0002.*

Murphy, B. (2015), Coseismic landslides. *Landslide Hazards, Risks and Disasters* (pp. 91-129). Academic Press. https://doi.org/10.1016/B978-0-12-396452-6.00004-5.

Nissen, E., Ghods, A., Karasözen, E., Elliott, J.R., Barnhart, W.D., Bergman, E.A., et al. (2019), The 12 November 2017 M w 7.3 Ezgeleh-Sarpolzahab (Iran) Earthquake and Active

Tectonics of the Lurestan Arc. *Journal of Geophysical Research: Solid Earth, 124(2),* 2124-2152. https://doi.org/10.1029/2018JB016221.

Roback, K., Clark, M.K., West, A.J., Zekkos, D., Li, G., Gallen, S.F., Chamlagain, D., & Godt, J.W. (2018), The size, distribution, and mobility of landslides caused by the 2015 Mw7.8 Gorkha earthquake, Nepal. *Geomorphology, 301*, 121-138. https://doi.org/10.1016/j.geomorph.2017.01.030.

Roberts, N. J., & Evans, S. G. (2013), The gigantic Seymareh (Saidmarreh) rock avalanche, Zagros Fold–Thrust Belt, Iran. *Journal of the Geological Society, 170(4),* 685-700. doi:10.1144/jgs2012-090.

Rojstaczer, S., & Wolf, S. (1992), Permeability changes associated with large earthquakes. An example from Loma Prieta, California. *Geology, 20(3)*, 211-214. https://doi.org/10.1130/0091-7613(1992)020<0211:PCAWLE>2.3.CO;2.

Rosen, P.A., Hensley, S., Peltzer, G., & Simons, M. (2004), Updated repeat orbit interferometry package released. *Eos Transactions American Geophysical Union, 85(5*), 47-47. https://doi.org/10.1029/2004EO050004.

Schulz, W.H., McKenna, J.P., Kibler, J.D., & Biavati, G. (2009), Relations between hydrology and velocity of a continuously moving landslide-evidence of pore-pressure feedback regulating landslide motion?. *Landslides, 6,* 181–190. https://doi.org/10.1007/s10346-009-0157-4.

Tanyas, H., Van Westen, C.J., Allstadt, K.E., Anna Nowicki Jessee, M., Görüm, T., Jibson, R.W., et al. (2017), Presentation and analysis of a worldwide database of earthquake-induced landslide inventories. *Journal of Geophysical Research: Earth Surface, 122(10),* 1991-2015. https://doi.org/10.1002/2017JF004236.

Tavani, S., Mariano Parente, M., Puzone, F., Corradetti, A., Gharabeigli, G., Valinejad M., et al. (2018), The seismogenic fault system of the 2017 Mw 7.3 Iran–Iraq earthquake: constraints from surface and subsurface data, cross-section balancing, and restoration. *Solid Earth*, *9*, 821–831. https://doi.org/10.5194/se-9-821-2018.

Vajedian, S., Motagh, M., Mousavi, Z., Motaghi, K., Fielding, E., Akbari, B., et al. (2018), Coseismic deformation field of the Mw 7.3 12 November 2017 Sarpol-e Zahab (Iran) earthquake: A decoupling horizon in the northern Zagros Mountains inferred from InSAR observations. *Remote Sensing*, *10(10)*, 1589. doi:10.3390/rs10101589.

Valkaniotis, S., Ganas, A., Tsironi, V., & Barberopoulou, A. (2018), A preliminary report on the M7.5 Palu 2018 earthquake co-seismic ruptures and landslides using image correlation techniques on optical satellite data. *EMSC*. https://doi.org/10.5281/zenodo.1467128.

Wang, C. Y., & Chia, Y. (2008), Mechanism of water level changes during earthquakes: Near field versus intermediate field. *Geophysical Research Letters, 35,* L12402. doi:10.1029/2008GL034227.

Wang, G., Zhang, D., Furuya, G., & Yang, J. (2014), Pore-pressure generation and fluidization in a loess landslide triggered by the 1920 Haiyuan earthquake, China: a case study. *Engineering Geology*, *174,* 36-45. https://doi.org/10.1016/j.enggeo.2014.03.006.

Zerathe, S., Lacroix, P., Jongmans, D., Marino, J., Taipe, E., Wathelet, M., et al. (2016), Morphology, structure and kinematics of a rainfall controlled slow-moving Andean landslide, Peru. *Earth Surface Prosses and Landforms*, *41(11)*, 1477-1493. https://doi.org/10.1002/esp.3913.

Supporting Information References

Geli, L, Bard, P.Y., & Jullien, B. (1988), The effect of topography on earthquake ground motion: A review and new results. *Bulletin of the Seismological Society of America, 78 (1)*, 42–63.

Kramer, S. L. (1996). Geotechnical earthquake engineering. In *Prentice–Hall international series in civil engineering and engineering mechanics* (Chapter 6, pp. 226– 228). New Jersey: Prentice-Hall.

Socco, L. V., Jongmans, D., Boiero, D., Stocco, S., Maraschini, M., Tokeshi, K., & Hantz, D. (2010), Geophysical investigation of the Sandalp rock avalanche deposits. *Journal of Applied Geophysics, 70(4*), 277-291. https://doi.org/10.1016/j.jappgeo.2009.12.005.

Telford, W.M., Geldart, L.P., Sheriff, R.E., & Sheriff, R.E. (1990), *Applied geophysics*. London:Cambridge university press. doi:10.1017/CBO9781139167932.

AGU PUBLICATIONS

Geophysical Research Letters

Supporting Information for

Far-field coseismic forcing of giant rockslides in the 2017 Sarpol-Zahab Earthquake (Iran)

Aya Cheaib[1,3], Pascal Lacroix[1], Swann Zerathe[1], Denis Jongmans[1], Najmeh Ajorlou[2], Marie-Pierre Doin[1], James Hollingsworth[1], and Chadi Abdallah[3]

1. ISTerre - Université Grenoble Alpes, IRD, CNRS, IFSTTAR, Université Savoie Mont Blanc, CS 40700, 38058 GRENOBLE Cedex 9 Grenoble, France.

[2]Department of earth science, Institute for Advanced Studies in Basic Sciences(IASBS), 444 Prof. Yousef Sobouti Blvd., Zanjan 45137-66731, Iran.

[3]Lebanese National Council for Scientific Research/Remote Sensing Center, Blvrd Sport City, Bir Hassan, P.O. Box 11-8281, Beirut, Lebanon.

Contents of this file

Additional Supporting Information (Files uploaded separately)

Captions for Table S2 (larger than 1 page, upload as separate file)

Introduction

This document provides supplementary information on the used data and methods, the uncertainty analysis presented in the main text, an extended description of the results and detailed explanation of the giant rockslides site effect assessment.

As our study area is large and partially not well documented (Iran-Iraq boundary/area of conflict), the available geological maps were only: (1) a large geological map (1:2,500,000) for the entire Iran and (2) a 1:250,000 geological map for the Ilam province in Iran (southern far field of the earthquake). No geological maps were available for Iraq (see more details in text S1 and Figure S1).

Text S1. Data Set

Three kinds of DEMs were used in our study: (1) the ASTER GDEM of 30 m resolution (regional view of our study area), (2) 4 m resolution pre and post-earthquake DEMs (Table S1) that were generated in the region of the epicenter (Figure S1) from tri-stereo pairs of SPOT6-7 images using Ames-Stereo Pipeline (Beyer et al., 2018) , and finally (3) a 4 m resolution pre-earthquake DEM (also generated with Ames-Stereo Pipeline using tri-stereo SPOT7 images (acquired in 2014) covering the southern part of our study area, in the region of the far southern rockslides, Figure S1). See Table S1 for more details on the data.

SPOT data was provided via the CNES-funded ISIS program (now integrated with DINAMIS: Dispositif Institutionnel National d'Approvisionnement Mutualisé en Imagerie Spatiale).

The pre- and post-earthquake SPOT6-7 images (around the epicenter, Figure S1) of 1.5 m resolution were othorectified using the high resolution DEMs generated from the same data.

The PlanetScope images are available as orthorectified tiles, 10 km long and 25 km wide containing four bands (blue, green, red and infrared).

The 72 Sentinel-1 images cover 10 months before and after the earthquake. They were acquired from ESA with Interferometric Wide Swath (IW) mode from both A and B satellites and feature a 250 km swath, a spatial resolution of 5x20 m and a repeat cycle of 12 days.

A 1:2,500,000 regional geological map of the Iran republic (National Iranian Oil Company, NIOC) was used in our study, alongside a more detailed 1:250,000 geological map (Llewellyn, 1974), covering the Ilam region in Iran (Figure S1).

Text S2. Methods

Our working strategy aimed at detecting the maximum possible number of earthquake-induced landslides in our study area, extending 200+ km along the Iran-Iraq border. Thus, we used different methods: the scars of rapid coseismic landslides were mapped by a comparison of pre- and post-seismic Planet-scope images (Manual **visual comparison**), whereas slow-moving landslides (m/yr-mm/yr) were detected by deriving the ground deformation from optical (**Optical images correlation**) and radar (**Interferometric Synthetic Aperture Radar**) satellite images.

2.1. Visual comparison

To detect the rapid slope-failures, the available pre- and post-earthquake PlanetScope data were merged then compared in ArcGIS software using the **"swipe"** tool. To accomplish this inventory in the best way, we used the available DEMs and the earth view base maps in order to verify that the detected landslide scars occur on topographic slopes and try to visualize them if possible.

2.2. Optical image correlation

The COSI-CORR iterative correlator was used to measure the horizontal displacements on the Earth's surface using georeferenced optical images (Leprince et al., 2007). Each correlation yields a north-south and an east-west displacement fields, as well as a signal to noise ratio map. It allows usually the detection of displacements higher than 10% of the image's pixel resolution during the time interval between the two correlated images.

First we correlated the mosaic of SPOT6-7 images covering the area around the epicenter (a minimum distance of 10 km and a maximum distance 75 km to the epicenter). The correlation was conducted pixel by pixel in the frequency domain using a sliding window of 64 pixels in both iterations.

In a second step we correlated the available PlanetScope images in the southern part of our study area (see Figure S1). The aim of this step is to see if we can detect any displacement fields on the body of the rockslides detected from the coseismic interferograms. Thus, the green bands were correlated in the frequency domain for each pixel using a sliding window of 64 pixels also for both iterations.

Each time, several tests were done before adopting the final sliding window sizes.

The obtained results were then detrended in ENVI software and corrected afterward with Matlab by eliminating the pixels of high signal to noise ratios then subtracting the median of all the displacement field from each pixel.

2.3. Interferometric Synthetic Aperture Radar (InSAR)

We generated differential interferograms using NSBAS (New Small BAseline Subset) (Doin et al., 2011) process chain based on the ROI_PAC software (Rosen et al., 2004). See more details in the manuscript.

Text S3. Results

In total, 369 earthquake-induced landslides were detected. We divided them into two main categories: rockfalls and giant rockslides.

3.1. Rockfalls

360 scars of rockfalls were mapped around the epicenter using the visual comparison of Planet-scope images. In the following figures we will be showing an example of how we detected the scars of the debris cones (Figure S2), their density analysis (Figure S3) and their occurrence on the available slopes (Figure S4).

3.2. Giant rockslides

9 giant rockslides were detected. One of them was the Mela-kabod rockslide detected from optical images correlation that moved coseismically for about 35 m toward the south-west (Figure S5). While 8 landslide-like patterns were detected from the coseismic interferograms (Figure 2) and then interpreted to be old giant rockslides. The characteristics of all the rockslides are detailed in Table S2 and presented in Figure S6.

However, in Ghazipur and Simpson (2016), the areas of those rockslides are systematically underestimated by up to an order of magnitude compared to the surface areas determined from our results (Table S2).

Text S4. Quantification of Giant Rockslides Coseismic Displacement

While a coseismic movement of all the rockslides is observed in the coseismic interferograms (Figure 2), its precise quantification is not possible due to (1) the sharp limits of the patterns in the coseismic interferograms, that prevent extraction of the phase ambiguity during the unwrapping process, and (2) the absence of pattern in the correlation of optical images. However, those two sources of data nevertheless provide constraints on the coseismic movement between several cm (~10 cm) in the radar LOS and 0.9 m maximum for all the rockslides (Table S2). The minimal coseismic displacement can be quantified by counting the number of fringes inside each rockslide pattern (formula: (number of fringes*wave length)/4pi). The maximum value of the coseismic displacement can be estimated by the uncertainty of the horizontal displacement field obtained from optical PlanetScope images correlation (explained above).

Text S5. Time-series analysis

After detecting and characterizing the slow movements triggered by the Sarpol-Zahab earthquake in our study area, we computed their radar LOS time-series for each pixel in the interferograms stack over 10 months before and after the earthquake. To do that, we divided the interferograms into pre- and post-earthquake groups, then we inverted the phase delays of the unwrapped interferograms pixel by pixel in order to solve the total phase delay, relative to the first date (Doin et al., 2011). Time-series were then constructed in Matlab using the cumulative deformation maps obtained from the inversion (one map at each date of the Sentinel-1 images). So we calculated the mean displacement over a selected window, of about 25x25 pixels on the landslide body at each date, relative to a mean displacement extracted from a surrounding stable area of hundreds of meters around it. The final displacement was computed from the differences between the two means. After that, the deviation of the displacement was estimated from the mean absolute deviation of the displacement in the reference area.

In a next step, we calculated the pre-and post-seismic landslide mean velocities and their associated uncertainties. Each point "i" of the time-series is considered as a random variable of normal distribution (mu_i, sigma_i). 10,000 realizations of this random variable are randomly picked at each point of the time series, and the associated 10,000 pre and post velocities are calculated by a linear regression with time. The mean and standard deviation of these 10,000 velocities gives us an estimate of the mean velocity and its uncertainty.

Text S6. Site Effect Assessment of the Giant Rockslides

Six of the giant landslides affected the same 200 m thick Ilam formation (limestone) overlying a 100 m thick shale layer (Surgah formation). This structure constitutes a dynamic oscillator on the thick carbonate Sarvak formation.

During the slide of the rockslides, the block disintegrated and dragged part of the Surgah formation, creating a highly destructive deposit with a maximum thickness *t* of around 150 m, consisting of a mixture of shale and limestone. The amplification of the seismic waves resulting from the earthquake is due to the seismic impedance contrast (product of the density ρ and shear wave velocity Vs) between this deposit and the underlying, mainly calcareous, substratum. For vertically incident waves and 1D structure, the resonance frequency f_o and the corresponding amplification Af_o are given by (Kramer, 1996):

$$f_0 = \frac{Vs_D}{4\,t} \qquad (1)$$

$$Af_0 = \frac{\rho_B\, Vs_B}{\rho_D\, Vs_D} \qquad (2)$$

where Vs_D and Vs_B are the shear wave velocities of the rockslide deposit and the bedrock, respectively, and ρ_D and ρ_B are the corresponding densities.

Rockslide deposit and bedrock Vs values at these sites are not available, but plausible values can be taken from a similar rockslide for the deposit mixing limestone and marl (Socco et al., 2010) and in the literature for bedrock (Telford et al., 1990):

Vs_D= 600 m/s ; Vs_B= 3000 m/s : ρ_D= 1.9 ; ρ_B= 2.5.

Considering these values, we obtain a resonance frequency $f_o \approx 1$ Hz associated to a 1D amplification over 6.

Thus the 1D resonance frequency of the carbonate Sarvak formation before the rockslide can be estimated to be around 1 Hz, taking plausible values of dynamic material moduli. After the rockslide, the destructured slump body, characterized by lower rigidity and smaller thickness (varying between 75 m and 150 m), also has a resonance frequency in the low range (1-2 Hz). Topographic amplification is maximum for a wavelength comparable to the width of the mountain (Geli et al., 1988), a condition that is again fulfilled in the low frequency range (around 1 Hz) if we consider a mountain a few km wide with a velocity Vs of the order of 3 km/s. These results suggest that ground motion parallel to the slope may have been significant around 1 Hz at these 6 sites during the Sarpol-Zahab earthquake, due to the combined effect of a particular directivity of the source and site amplification that can generate ground motions 5 to 10 times stronger than normal (Murphy, 2015). Interestingly, the presence of multiple ridges can even increase the topographic effect (Geli, et al, 1988).

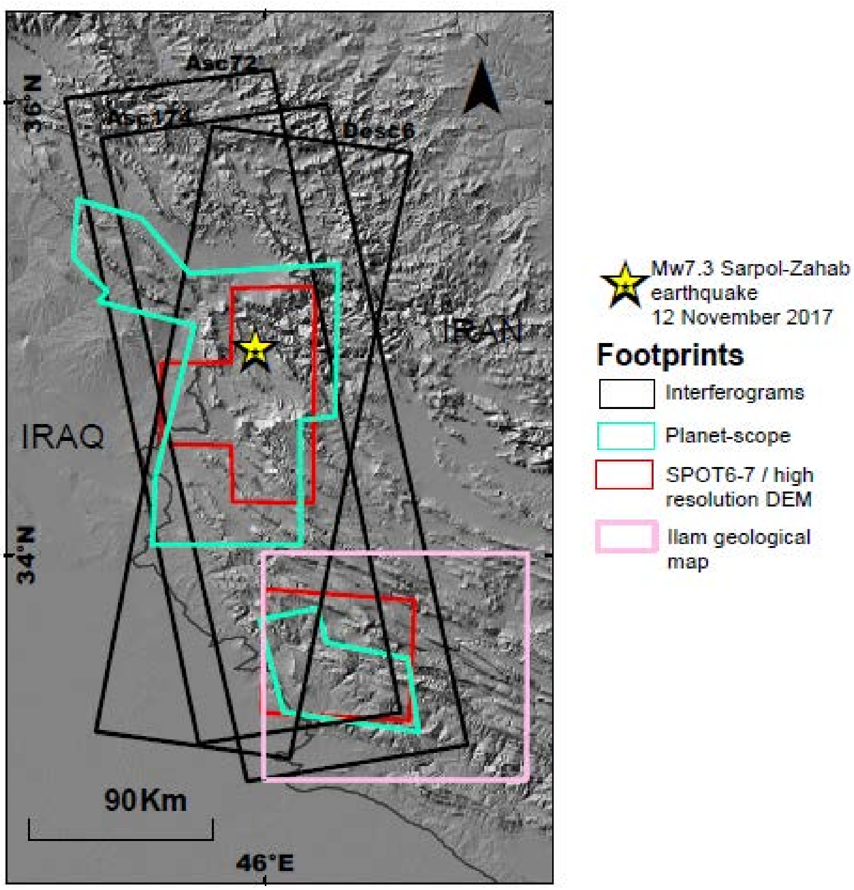

Figure S1. Footprints of the data used in our study. When pre- and post-earthquake data are available, the common area is presented.

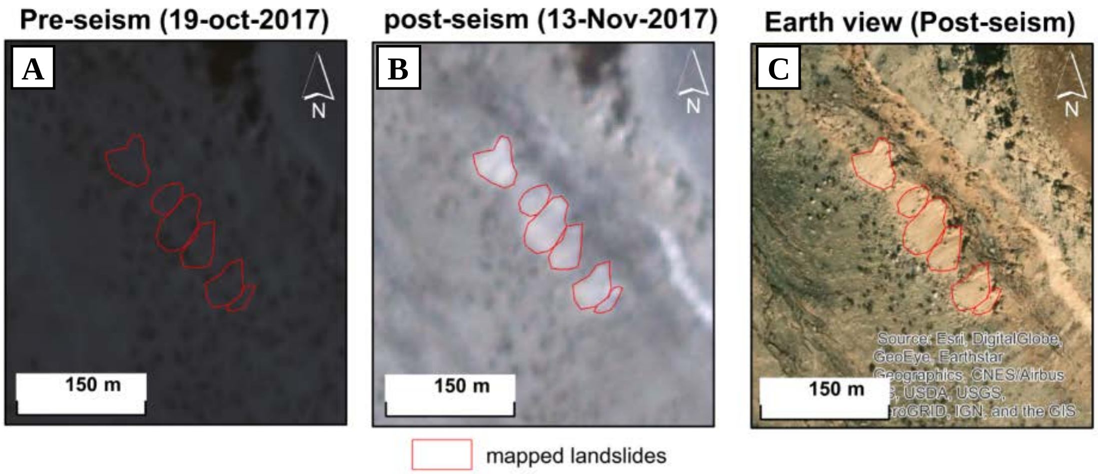

Figure S2. Typical example of rapid landslides mapped from PlanetScope images (3 m resolution). (A) and (B) show the view of the same area from PlanetScope images before and after the Sarpol-Zahab earthquake respectively. (C) shows the Google Earth view of the same extent.

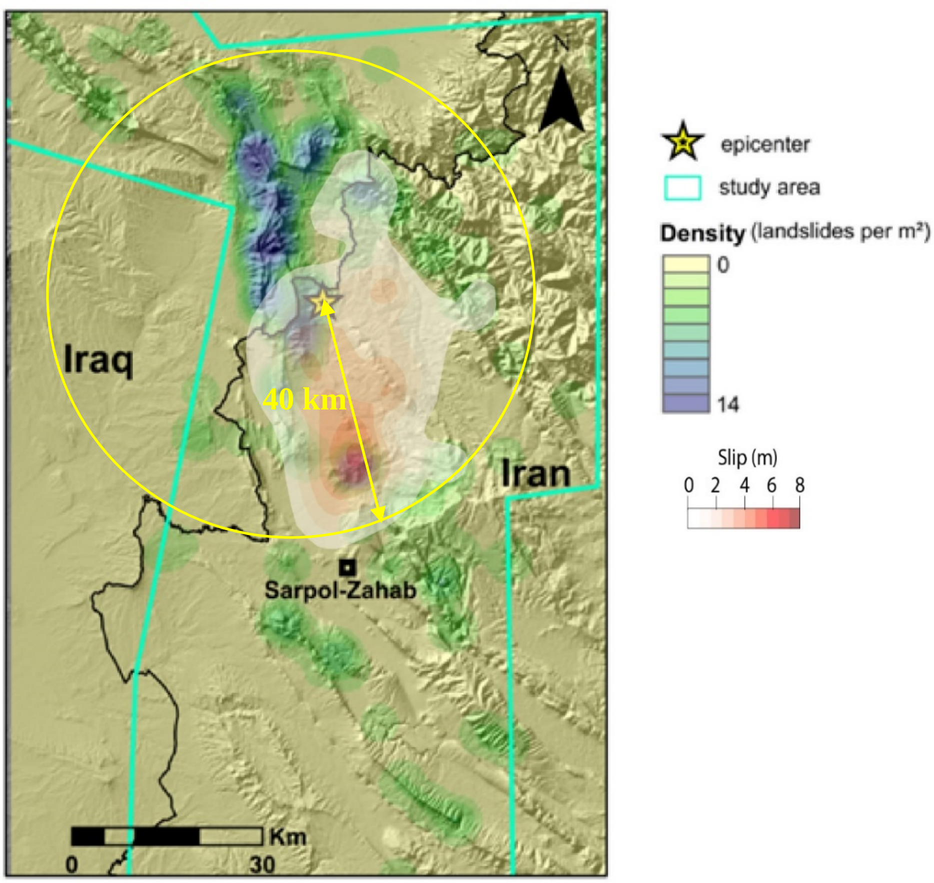

Figure S3. Rapid rockfalls density map. This map was calculated using the Kernel density tool in ArcGIS software by evaluating the density of points within a 5 km radius. The cumulative slip at 12 s was added from Gombert et al (2019).

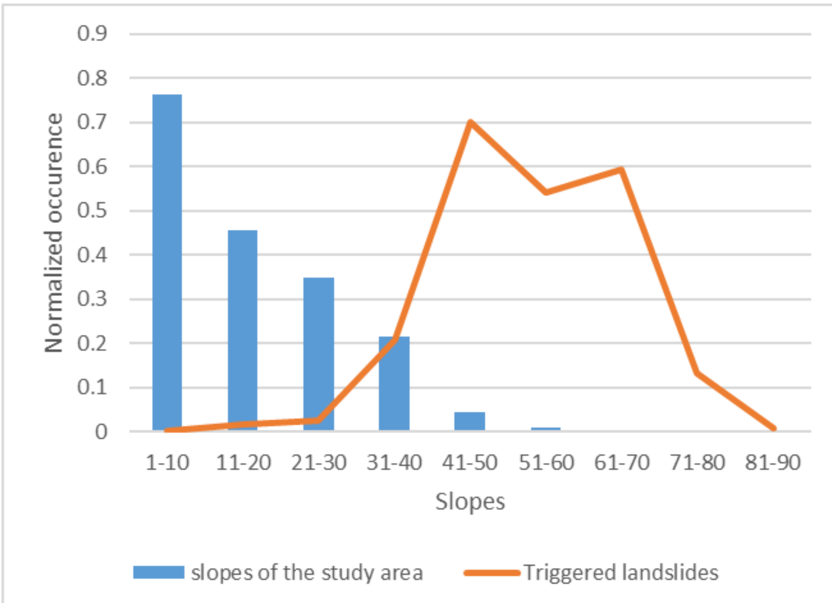

Figure S4. Plot showing the distribution of 276 detected rockfalls in respect to the available slopes of our study area.

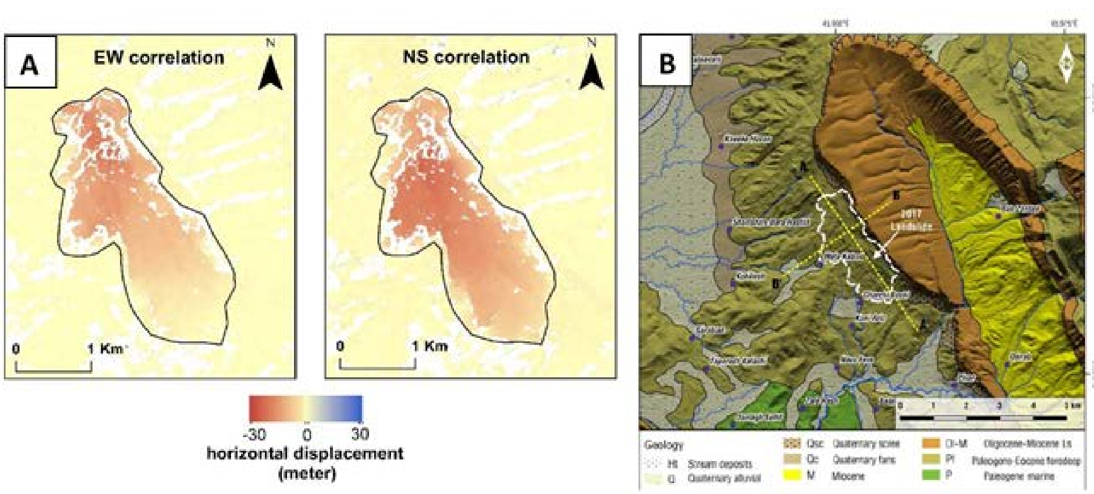

Figure S5. (A) Spot-6 images (Table S1) correlation results for the Melah-Kaboud landslide obtained using the COSI-Corr tool, showing the coseismic displacement during the Sarpol-Zahab earthquake. (B) Geological map of the Mela-Kaboud landslide region from the study of

Valkaniotis et al (2018). The white contour shows the limit of the displacement field detected from high resolution images in their study.

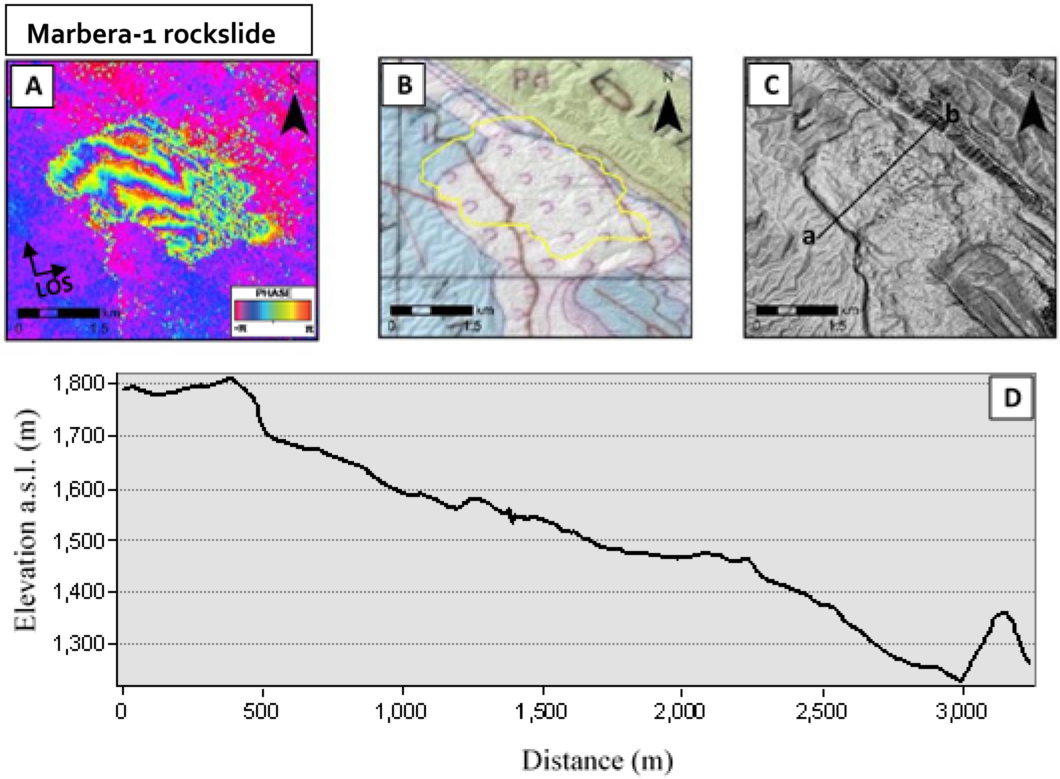

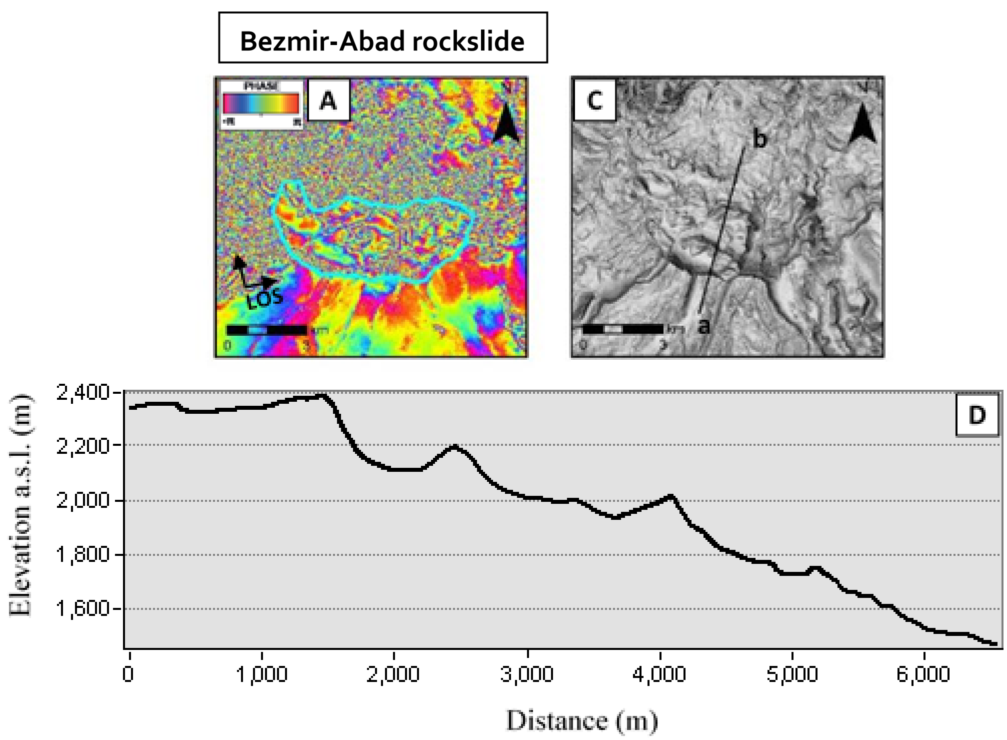

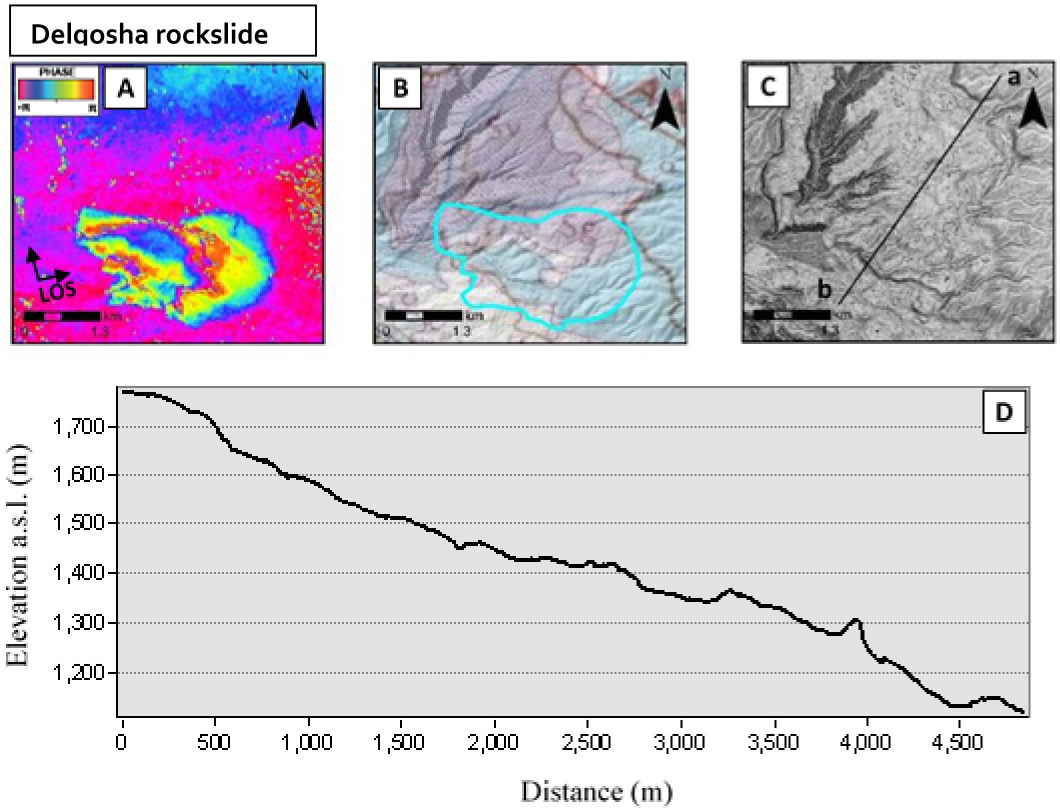
Delgosha rockslide
A
B
C
D
LOS
a
b
Elevation a.s.l. (m)
Distance (m)
1,700
1,600
1,500
1,400
1,300
1,200
0
500
1,000
1,500
2,000
2,500
3,000
3,500
4,000
4,500

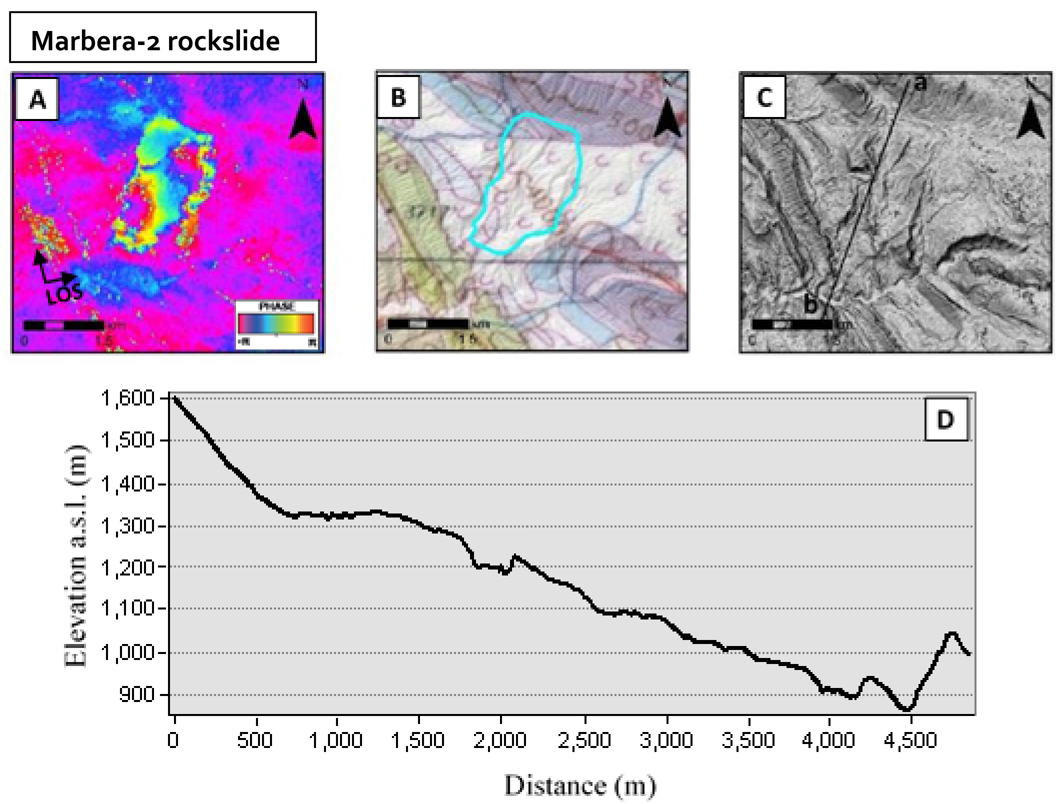
Marbera-2 rockslide
A
B
C
D
LOS
a
b
Elevation a.s.l. (m)
Distance (m)
1,600
1,500
1,400
1,300
1,200
1,100
1,000
900
0
500
1,000
1,500
2,000
2,500
3,000
3,500
4,000
4,500

Marbera-3 rockslide

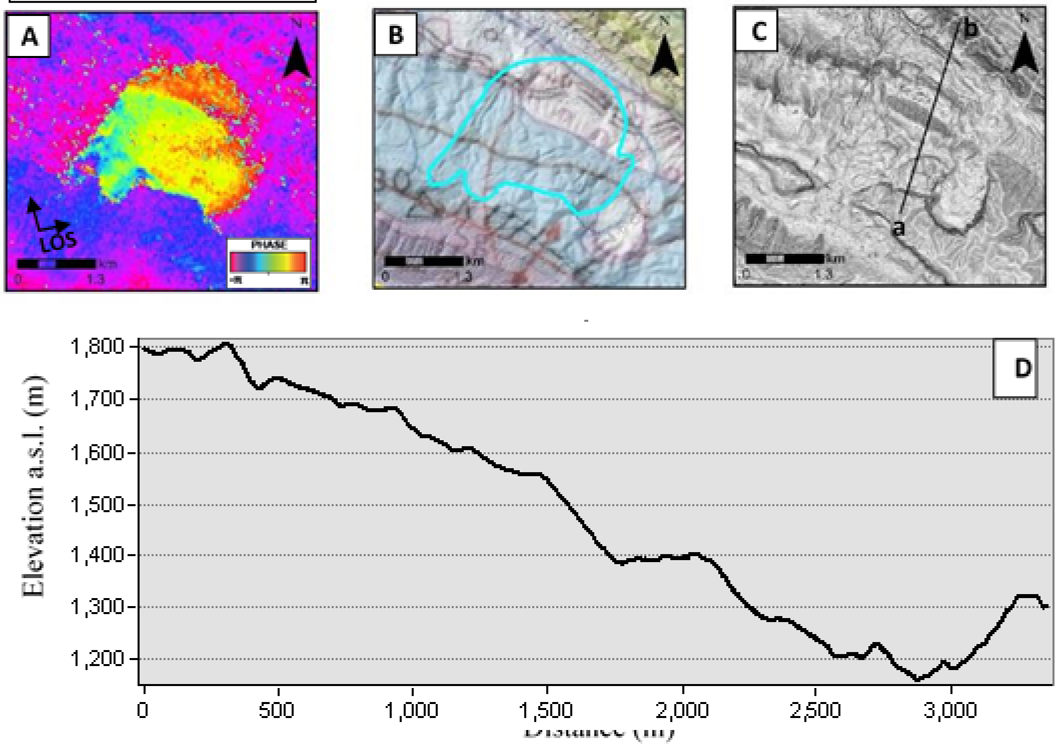

Sarney-1 rockslide

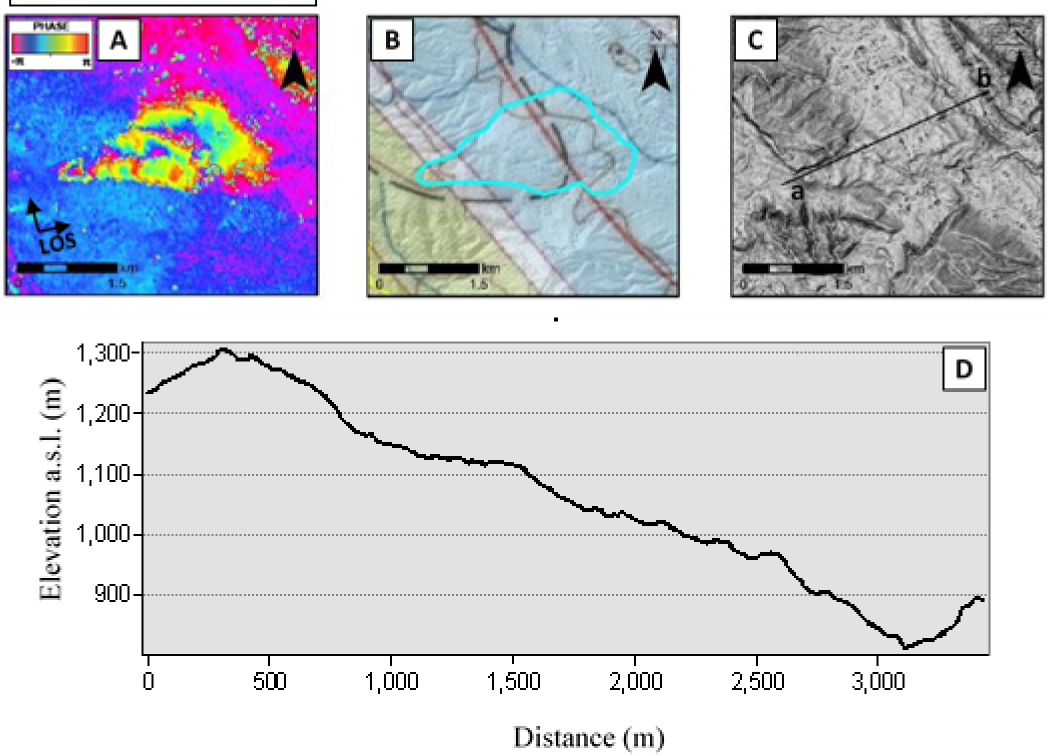

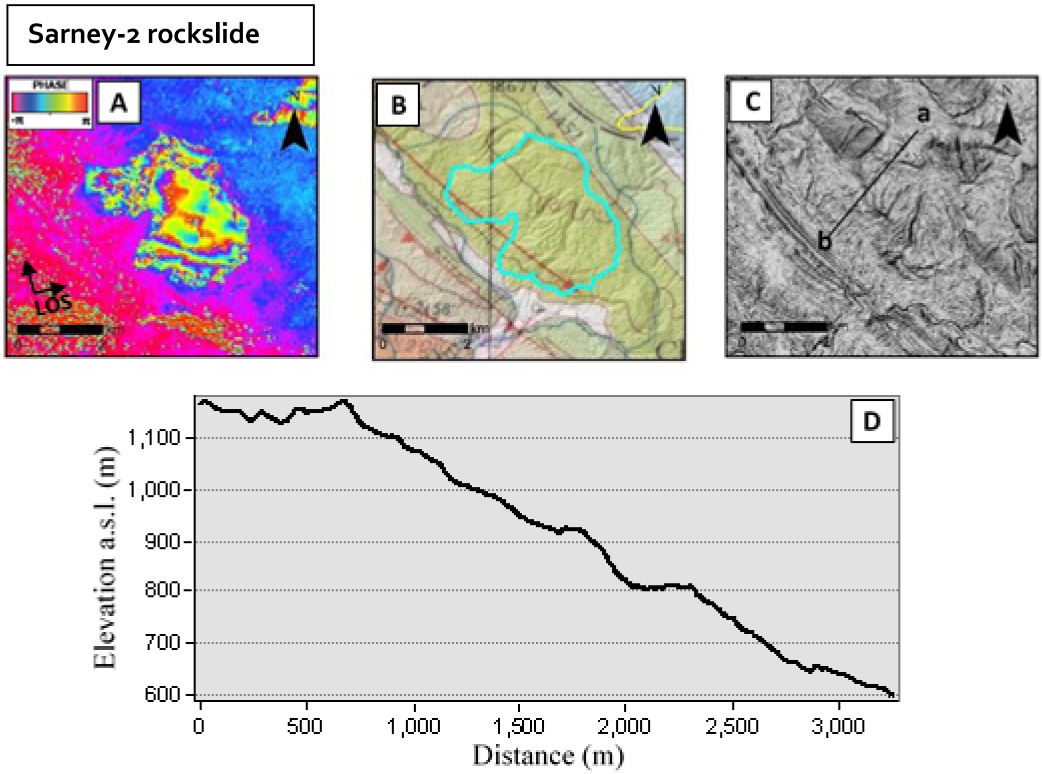

Figure S6. Figures showing (A) the interferogram pattern (the interferogram is computed along the ascending track 72 between 11/11/2017 and 17/11/2017), (B) the geological map, (C) the DEM and (D) a topographic profile 'ab' along the instance of the rockslides (other than the

Mehr rockslide). No detailed geological map is available for the region around the epicenter (the region of the Bezmir-Abad and Mela-Kaboud landslide).

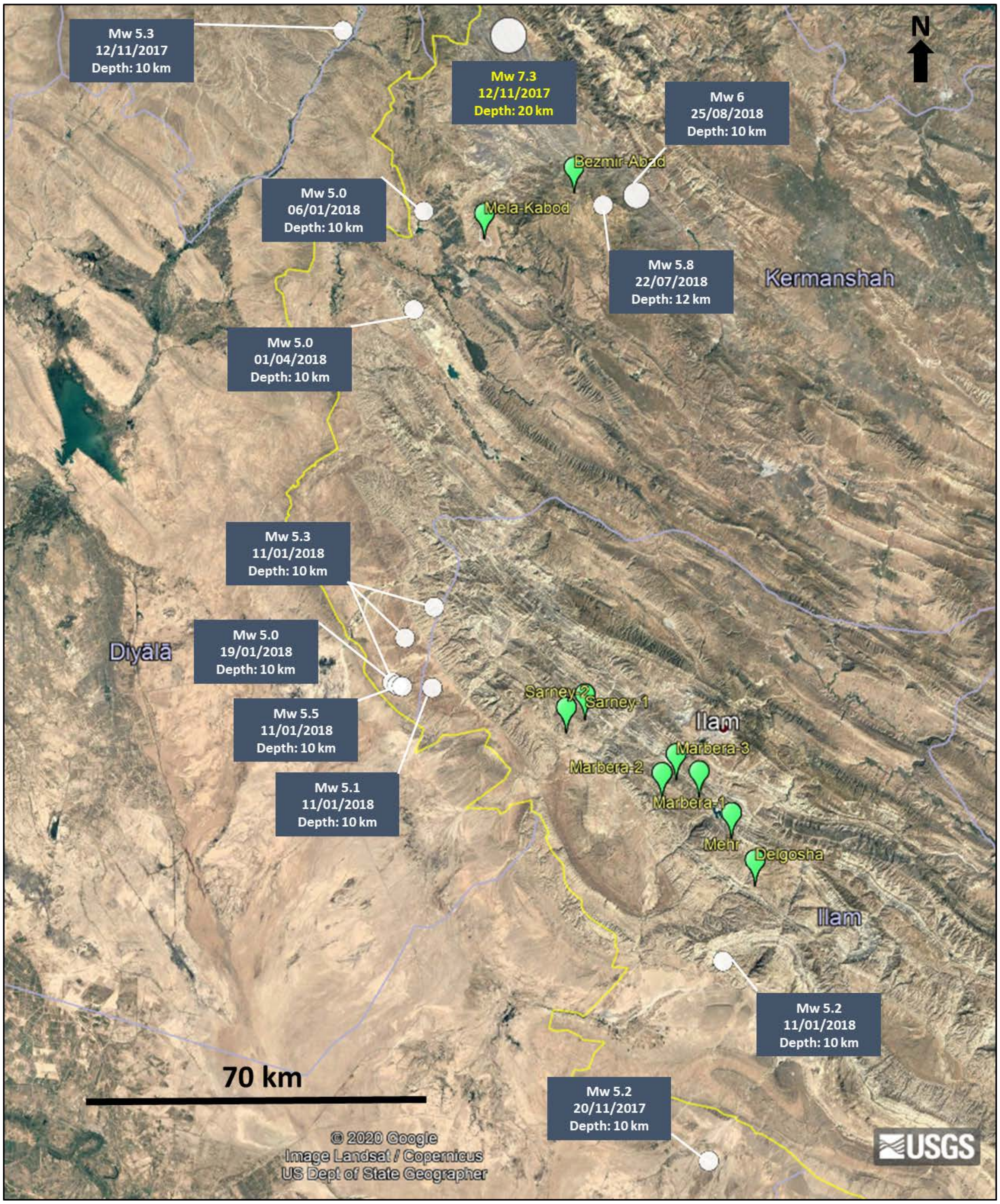

Figure S7. Details of all the seismic events that took place during the period of the accomplished time-series analysis (10-01-2017 and 27-08-2018).

<table>
<tr><th colspan="2" rowspan="2">Data type and origin</th><th colspan="2">Date of acquisition</th><th rowspan="2">Resolution (meter)</th><th rowspan="2">Application and use</th></tr>
<tr><th>Pre-earthquake</th><th>Post-earthquake</th></tr>
<tr><td rowspan="3">Optical</td><td rowspan="2">PlanetScope</td><td>19-Oct-2017 (North*)</td><td>13-Nov-2017 (North*)</td><td>3 m</td><td rowspan="2">-Image correlation (COSI-Corr)
-Visual comparison</td></tr>
<tr><td>07-Nov-2017 (South*)</td><td>17-Nov-2017 (South*)</td><td>3 m</td></tr>
<tr><td>Spot-6</td><td>13-Oct-2013, 24-Apr-2014 , 04-May-2014, 14-Aug-2014</td><td>29-Nov-2017 , 12-Dec-2017</td><td>1 m</td><td>-Image correlation (COSI-Corr)
- Dem generation</td></tr>
<tr><td>Radar</td><td>Sentinel-1 AB</td><td>10-Jan-2017 to 06-Nov-2017 (repeat cycle each 12 days)</td><td>12-Nov-2017 to 27-Aug-2018 (repeat cycle each 12 days)</td><td>5x20 m</td><td>New Small BAseline Subset (NSBAS)</td></tr>
<tr><td rowspan="3">Digital Elevation Models</td><td>ASTER</td><td colspan="2">---------------------------</td><td>30 m</td><td>Correction of interferograms</td></tr>
<tr><td rowspan="2">Spot-6/7</td><td>13-Oct-2013, 24-Apr-2014, 04-May-2014, 14-Aug-2014</td><td>29-Nov-2017, 12-Dec-2017</td><td>2 m</td><td rowspan="2">-Interpretation of landslides
-Generation of cross-sections</td></tr>
<tr><td colspan="2">09-Nov-2014 (south*)</td><td>4 m</td></tr>
</table>

North*correspond to the area around the epicenter

South* correspond to the area of the rockslides detected in the far field to the south from the epicenter

Table S1. Synthesis of satellite data used in this study and their characteristics.

Table S2. Characteristics of the giant slow-moving rockslides detected from Sentinel-1 interferograms and optical images correlation. The area of the rockslides already identified by Ghazipur and Simpson (2016) is given for comparison. The area deduced from this study corresponds to the area of the interferogram (see Results for details). The volume is calculated based on the empirical law adopted in the study of Ghazipur and Simpson (2016) for the Zagros region. ΔH is the elevation difference between the landslide toe and its headscarp. The average slope is calculated from the headscarp top to the landslide toe. Landslide orientation gives the direction toward which the landslide is sliding; “North-East” means the landslide orientation is from South-West to North-East. Line Of Sight (LOS) velocities correspond to linear interpolation of accumulated displacements from time-series computed over several months (see Figure 4 and text S5 for details).